Editors' Suggestion

Spin-lattice entanglement in $CoPS_3$

Thuc T. Mai,[1,2,3,*] Amber McCreary,[1] K. F. Garrity,[4] Rebecca L. Dally,[5] Sambridhi Shah,[6] Bryan C. Chakoumakos,[7] Md Nasim Afroj Taj,[8] Jeffrey W. Lynn,[9] Michael A. McGuire,[10] Benjamin S. Conner,[2,11] Mona Zebarjadi,[12] Janice L. Musfeldt,[6,13] Angela R. Hight Walker,[1] Rahul Rao,[2] and Michael A. Susner[2,†]

[1]*Quantum Measurement Division, Physical Measurement Laboratory, NIST, Gaithersburg, Maryland 20899, USA*
[2]*Materials and Manufacturing Directorate, Air Force Research Laboratory, Wright-Patterson Air Force Base, Ohio 45433, USA*
[3]*Bluehalo, LLC, 4401 Dayton-Xenia Rd, Dayton, Ohio 45432, USA*
[4]*Materials Measurement Science Division, Materials Measurement Laboratory, NIST, Gaithersburg, Maryland 20899, USA*
[5]*Sensor Science Division, Physical Measurement Laboratory, National Institute of Standards and Technology, Gaithersburg, Maryland 20899, USA*
[6]*Department of Chemistry, University of Tennessee, Knoxville, Tennessee 37996, USA*
[7]*Neutron Scattering Division, Oak Ridge National Laboratory, Oak Ridge, Tennessee 37830, USA*
[8]*Electrical and Computer Engineering Department, University of Virginia, Charlottesville, Virginia 22904, USA*
[9]*NIST Center for Neutron Research, National Institute of Standards and Technology, Gaithersburg, Maryland 20899, USA*
[10]*Materials Science and Technology Division, Oak Ridge National Laboratory, Oak Ridge, Tennessee 37831, USA*
[11]*Azimuth Corporation, 2079 Presidential Drive, No. 200, Fairborn, Ohio 45342, USA*
[12]*Electrical and Computer Engineering Department, Materials Science and Engineering Department, University of Virginia, Charlottesville, Virginia 22904, USA*
[13]*Department of Physics and Astronomy, University of Tennessee, Knoxville, Tennessee 37996, USA*

(Received 16 June 2025; revised 27 August 2025; accepted 18 September 2025; published 16 December 2025)

Complex chalcogenides in the MPS_3 family of materials (M = Mn, Fe, Co, and Ni) display remarkably different phase progressions depending upon the metal center orbital filling, character of the P–P linkage, and size of the van der Waals gap. There is also a stacking pattern and spin-state difference between the "lighter" and "heavier" transition-metal-containing systems that places $CoPS_3$ at the nexus of these activities. Despite these unique properties, this compound is underexplored. Here, we bring together Raman scattering spectroscopy and infrared absorption spectroscopy with x-ray techniques to identify a structural component to the 119 K magnetic ordering transition. With temperature-dependent Raman scattering, we discover a set of magnon-phonon pairs that engages in avoided crossings below $T_{\text{Néel}}$. These findings point to strong spin-phonon entanglement as well as opportunities to control these effects under external stimuli.

DOI: 10.1103/nbp7-glqj

I. INTRODUCTION

Van der Waals (vdW) solids are superb platforms for exploring the interplay between structure and magnetism in reduced dimensions [1]. Complex chalcogenides in the MPX_3 family [2] are especially interesting because they host extensive chemical and physical tunability. Here, M is a transition metal, P is phosphorus, and X is either sulfur or selenium. For M = Mn, Fe, Co, and Ni, the system hosts a variety of antiferromagnetic (AFM) arrangements ranging from zigzag Ising AFM order in $FePX_3$ to in-plane zigzag AFM order in $CoPS_3$ and $NiPS_3$ to easy-plane Néel-type AFM order in $MnPSe_3$ [2]. At the single-ion level, the 2+ charge on the metal ion results in a rich many-body electronic ground state. Examples include a pure spin configuration of $S = 5/2$ for Mn^{2+} and mixed spin-orbit coupled states including $S = 1$, $L = 3$ for Ni^{2+}, $S = 2$, $L = 1$ for Fe^{2+}, and $S = 3/2$, $L = 3$ for Co^{2+} [3]. Of all the MPX_3 compounds, $CoPS_3$ is one of the least studied members of this family of materials, primarily due to challenges with synthesis. It hosts AFM order below $T_N \approx 119$ K [4]. At the same time, spin-orbit coupling emanating from the Co^{2+} center is highly underexplored, although, based upon recent measurements of other honeycomb lattice magnets such as $CoTiO_3$ [5–7], the interaction is likely to impart additional functionality in the form of a rich magnetic excitation spectrum that can be described by both spin and orbital degrees of freedom. We therefore anticipate that spin-orbit coupling (SOC) will entangle the magnetic and crystalline structures in $CoPS_3$ in a meaningful and potentially useful manner.

Perhaps unsurprisingly, observations of spin-lattice coupling across the AFM transition temperatures have been reported for several members of the MPX_3 family, although only $FePS_3$ has been confirmed to exhibit a concomitant structural transition with its magnetic transition through diffraction [8,9] and calorimetric measurements [10]. Spectroscopic measurements on bulk crystals as well as mono- and few-layered MPX_3 materials have shown the appearance of new

*Contact author: thuc.mai.ctr@us.af.mil
†Contact author: michael.susner.2@us.af.mil

zone-folded phonon modes [11–13], increased two-magnon scattering, and Fano resonances below T_N [14,15], as well as strong variations in peak frequencies and intensities due to spin-lattice coupling [11,16,17]. The hybridization or entanglement between magnons and phonons below T_N was also reported for MPX_3 compounds [16,18–21]. Here, magnons and phonons are the quasiparticles that correspond to the magnetic and lattice excitations, respectively. Understanding their coupling is crucial for the realization of magnon-based computing technologies [22].

An inelastic neutron scattering study on $CoPS_3$ single crystals revealed four magnon branches at the Brillouin-zone center, with the lowest two being approximately 15 meV and 23 meV [23]. While significant overlap in the magnon and phonon energies was also reported, spin-lattice interactions were not considered. In this study, we observed two key and unambiguous signatures of spin-lattice coupling: magnetostriction and magnon-phonon hybridization.

We conducted detailed temperature-dependent Raman spectroscopy, IR spectroscopy, single-crystal x-ray diffraction (XRD), and high-resolution synchrotron powder XRD to characterize the lattice and magnetic excitation spectra of single-crystalline $CoPS_3$. The temperature-dependent powder XRD shows a subtle lattice contraction concomitant with the magnetic transition, which was further confirmed in our specific-heat measurements, highlighting the strong spin-lattice coupling in $CoPS_3$. We also observed two sharp peaks at $106.9\,cm^{-1}$ and $187.5\,cm^{-1}$ (13.3 meV and 23.2 meV, respectively) in the low-temperature (5 K) Raman data, corresponding to the two lowest zone-center magnons. Through the temperature-dependent Raman data, we discovered several unique features that can be explained by the hybridization of the magnons and the Raman-active phonons. Our study reveals in detail the specific interactions between lattice excitations and magnetic excitations, paving the way for future studies of the rich physics that awaits us at the two-dimensional (2D) limit of these layered magnetic materials.

II. METHODS

We synthesized single crystals of $CoPS_3$ using the general procedures given in [2,24,25]. We combined, in a near stoichiometric ratio (20% excess P), freshly reduced Co powder (Alfa Aesar Puratronic, 22 mesh, 99.998%), P chunks (Alfa Aesar Puratronic, 99.999%), and S chunks (Alfa Aesar Puratronic, 99.9995%) in an evacuated fused silica ampoule (20 cm length, 14 mm ID, 19 mm OD) together with ≈100 mg I_2 as a vapor transport agent. We then placed the ampoule into an MHI H-series tube furnace, ramped to the reaction temperature of 650 °C over 30 h, and held the reaction at that temperature for 100 h, after which we cooled to room temperature over an additional period of 30 h. The crystals we obtained were in the form of micaceous, flat platelets, < 0.5 mm thick, with the c axis aligned with the plane normal of the platelet. The largest crystals were ∼20 mm in diameter with most being in the 4 mm to 7 mm range.

Next, we confirmed the composition with scanning electron microscopy–energy-dispersive x-ray spectroscopy (SEM-EDS) analysis (3–4 spots per crystal for 9–12 spots total per batch) using a Thermo Scientific UltraDry EDS spectrometer joined with a JEOL JSM-6060 SEM. These results came out to, within error, the composition $CoPS_3$. We employed a Quantum Design MPMS-3 superconducting quantum interference device magnetometer to take magnetization measurements. Additionally, we collected XRD spectra off a flat crystal face (00l) using a Philips PANalytical system employing Cu K_α x-ray radiation at a wavelength of $\lambda_{K_{\alpha 1}} = 0.154\,056$ nm. We performed refinements on these data using FULLPROF [26] with LeBail fits to elucidate the layer spacing (here the monoclinic angle was set to 90°). We used a Quantum Design Dynacool PPMS instrument to measure specific-heat capacity data via pulsed calorimetry with a 2% heat rise. We also used the dual-slope analysis option with a 15% heat rise to probe possible phase transitions below T_N.

We performed single-crystal x-ray diffraction on a Rigaku XtalLAB Synergy S diffractometer equipped with a kappa-goniometer by using a Mo x-ray source. The data collection and reduction procedures were conducted in the CRYSALISPRO software [27]. High-resolution powder x-ray diffraction data were taken at the Advanced Photon Source synchrotron at Argonne National Laboratory on the beam line 11-BM. Single crystals of $CoPS_3$ were ground into a powder and encapsulated in a Kapton capillary which was placed into a closed-cycle cryostat reaching a base sample temperature of 6 K. Data were taken using a wavelength of $\lambda = 0.458\,122$ Å. The diffraction data were analyzed using a LeBail fit and the FULLPROF software [26], where the fit used the reflection conditions for the $C2/m$ space group.

For the temperature-dependent Raman measurements, we mounted a freshly cleaved bulk crystal inside a close-cycled optical cryostat in a helium gas environment. The sample temperature could be varied from 2 K to 300 K. The 633 nm excitation beam from a HeNe laser was incident onto the sample via free-space optics, through a 50X cryogenic objective. The laser spot size was approximately 1 μm. The backscattered beam was then collected and sent to a triple-stage spectrometer operating in triple-subtractive mode, which rejects the elastic light (Rayleigh scattering) and sends the Raman scattering to a liquid-nitrogen-cooled CCD. Various polarization optics were used to control the incident polarization and the scattered polarization. VV (VH) denotes the incident and scattered polarization being parallel (perpendicular) to each other. Polarization-resolved spectra were collected by placing a half-wave plate in the common beam path of the incident and scatter light, thus rotating both polarizations. This is equivalent to physically rotating the sample [28].

A single crystal of $CoPS_3$ was exfoliated between polypropylene tape to create a sample with appropriate optical density for our infrared (IR) spectroscopy experiments. We measured the far-IR transmittance using a Bruker 113v equipped with a helium-cooled bolometer detector and converted the transmittance to absorption. A continuous-flow cryostat provided temperature control.

We performed first-principles density functional theory (DFT) [29–31] calculations using the QUANTUM ESPRESSO code [32], with Garrity-Bennett-Rabe-Vanderbilt (GBRV) pseudopotentials [33]. We used the PBEsol exchange-correlation functional [34] and a Hubbard-U correction of 4 eV on the Co-d states (DFT+U) [35]. We used the PHONOPY

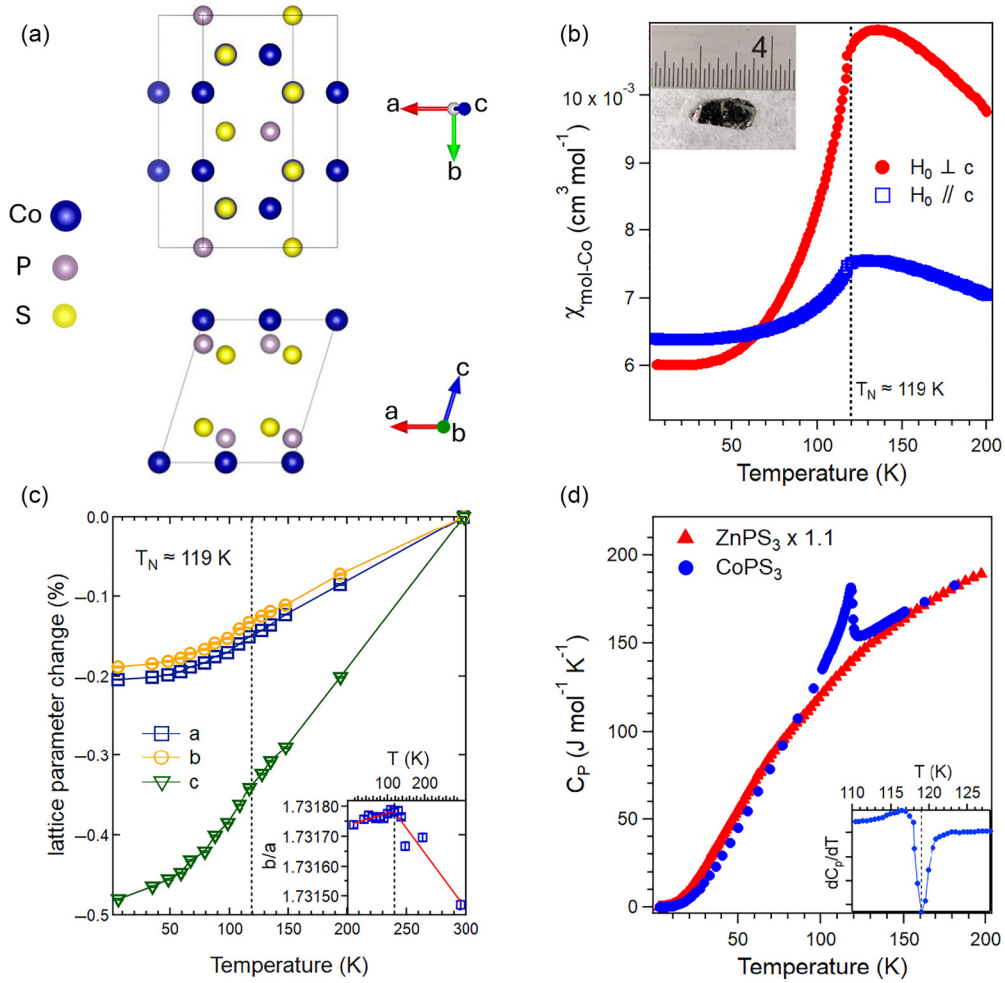

FIG. 1. Characterization of $CoPS_3$ single crystals. (a) Crystal structure views of the *a*-*b* plane (top) and *a*-*c* plane (bottom), with the monoclinic unit cell outlined. The images were generated with VESTA [37]. (b) Consistent with an earlier report [4], the magnetic susceptibility (M/H) as a function of temperature with T_N marking the onset of antiferromagnetic ordering. The inset shows a picture of a large single crystal. (c) From high-resolution synchrotron x-ray powder diffraction, the change in lattice parameters *a*, *b*, and *c* is shown across T_N. The inset shows the ratio of b/a, where the change in slope from above to below T_N can be seen by the phenomenological linear fits (red lines). (d) Specific heat of $CoPS_3$ showing a sharp peak also at T_N, with an inset showing the derivative of the heat-capacity curve. For comparison, the heat capacity of nonmagnetic $ZnPS_3$ is also shown. For both materials, 10 atoms per unit cell were used to obtain C_P.

code to calculate phonon frequencies and perform symmetry analysis [31,36].

III. RESULTS

The crystallographic and magnetization characterization results agree well with the existing literature for the single crystals used in our experiments [4]. The unit cell of $CoPS_3$ is shown in Fig. 1(a), where the monoclinic stacking along the *c* direction breaks the threefold rotation symmetry of the Co^{2+} honeycomb pattern in a single vdW layer. The inset of Fig. 1(b) shows a picture of one of our $CoPS_3$ single crystals, which typically grow to several mm in size. The temperature-dependent magnetic susceptibility of $CoPS_3$ points to an in-plane antiferromagnet, with the transition temperature being approximately 119 K [Fig. 1(b)], which is consistent with the literature [4]. The reported ordered moment is slightly greater than 3 μ_B, more than the spin-only contribution from the Co^{2+} ions [4], signifying an orbital component to the magnetism. Refined neutron diffraction analyzed in the critical regime from 109 K to T_N revealed that the critical exponent for the staggered magnetization is $\beta = 0.30(1)$, indicating that the order is more three dimensional than some of these vdW materials, but is well below the value for the isotropic Heisenberg model of $\beta = 0.365$ [4].

The room-temperature XRD pattern from an 00*L* face of a single crystal of $CoPS_3$ exhibits narrow linewidths, confirming the high crystal quality of our material (Fig. S1 in the Supplemental Material [39]). In addition, our initial single-crystal XRD measurements confirmed the $C2/m$ space group at three different temperatures: 95 K, 150 K, and 250 K, consistent with previously published studies [4,38,39]. We emphasize that the bulk $CoPS_3$ crystal lattice is monoclinic (point group C_{2h}), not hexagonal (D_{3d}), at room temperature and exhibits no evidence of *additional* rotational symmetry breaking across T_N.

In order to reveal the subtle temperature-dependent changes in lattice parameters, we performed a

higher-resolution study using a synchrotron source on a powder sample. In Fig. 1(c), we show the lattice parameters obtained from a LeBail fit of the high-resolution synchrotron data with respect to temperature using the reflection conditions for the $C2/m$ space group. The lattice parameters in Fig. 1(c) are expressed as a percentage of their values at 298 K, where $a = 5.899\,01(3)$ Å, $b = 10.213\,98(9)$ Å, $c = 6.666\,21(6)$ Å, and $\beta = 107.193\ 8(6)^\circ$ (uncertainties represent one standard deviation). As expected for a van der Waals material, the stacking direction c exhibits the largest change as the lamellae expand and contract, accordion like, with changing temperature. However, we note that near T_N, there is a subtle change in slope of the temperature dependence, depicted by the dashed vertical line in Fig. 1(c). A more dramatic change in slope is clearly shown in the evolution of b/a with temperature, where an inflection point is reached at T_N [inset in Fig. 1(c)].

The diffraction data of $CoPS_3$ point to the magnetostriction effect, where the onset of long-range magnetic ordering causes changes in the lattice parameters, reflected in the lattice expansion and contraction. This is consistent with a previous anisotropic magnetostriction measurement [40]. Further evidence for this structural component to the phase transition at T_N is given by an examination of the specific-heat capacity data of the magnetic transition [Fig. 1(d)]. Here we see a peak in the specific-heat capacity around T_N, where the ΔC_P at the transition is ≈36 J/(mol K). For comparison, in $FePS_3$, the antiferromagnetic transition is accompanied by a structural transition, leading to a ΔC_P of the same order of magnitude as our measurement [≈ 65 J/(mol K)] [10]. In contrast, ΔC_P in $MnPS_3$ was reported to be < 1 J/(mol K) at its magnetic transition temperature [10], where there is no evidence for a structural component to the magnetic transition. We also performed heat-capacity measurements on $ZnPS_3$, which is a paramagnetic sister compound to $CoPS_3$; this material does not exhibit any peaks across the same temperature range. The Debye temperature obtained from fitting C_P is approximately 325 K for $ZnPS_3$ and 340 K for $CoPS_3$. A recent report on $CoPS_3$ [24], using an IR reflection over a wide spectral range, showed that the Co^{2+} cation site symmetry is lowered when proceeding into the AFM state as the number of electronic absorption bands increased from 4 to 6; these data were correlated with a change in the temperature dependence of the layer spacing at T_N. These observations are suggestive of a subtle structural transition occurring at T_N involving the Co^{2+} cation.

Next, we discuss temperature-dependent Raman scattering across the phase transition. We observed drastic changes between the Raman spectra taken at 140 K and 5 K, above and below T_N [Fig. 2(a)]. The measured peak frequencies at 5 K are tabulated in Table I. Two very obvious differences between the high- and low-temperature spectra are the sharpness of the low-temperature peaks and the appearance of new modes. We labeled two new modes at low temperatures as M_1 and M_2, as they have the same energy as the zone-center magnons measured by inelastic neutron scattering [23].

Subtle differences in some phonon frequencies below and even above T_N between co- and cross-polarization configurations (VV and VH, respectively), can be seen in P_{11} and P_{12} [black arrow in Fig. 2(a)]. This behavior is the hallmark of

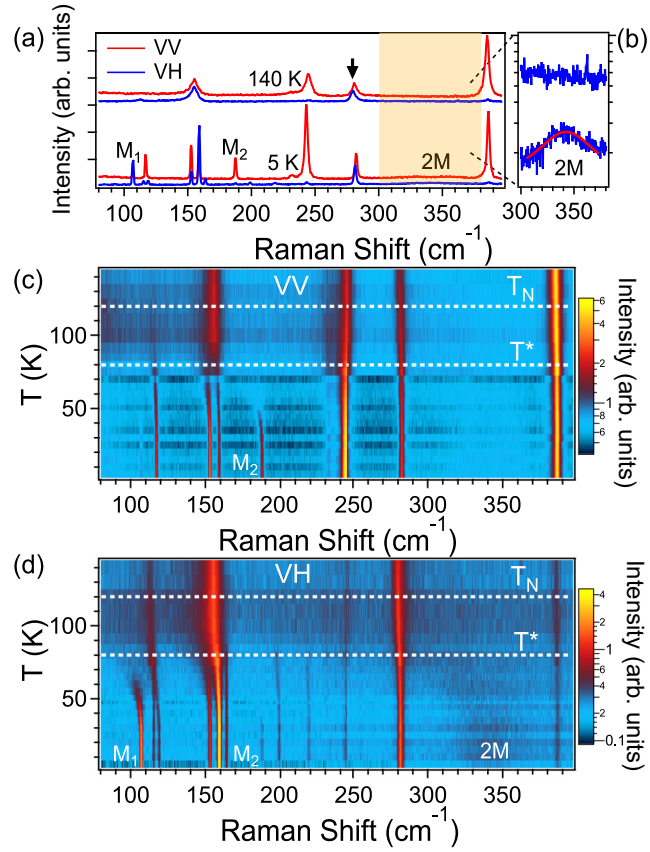

FIG. 2. Temperature-dependent Raman spectra from $CoPS_3$. (a) High (140 K) and low (5 K) Raman spectra of $CoPS_3$ are shown for parallel (VV) and crossed (VH) polarization, with offsets for clarity. The arrow points to a pair of A_g/B_g phonons with nearly degenerate frequencies, *above and below* T_N. Zone-center magnon modes are marked M_1 and M_2. The two-magnon scattering peak is labeled as 2M in the highlighted region between 300 cm^{-1} to 380 cm^{-1}. (b) A zoomed-in plot onto the 2M region, of the VH spectra at 140 K (above) and 5 K (below), with the intensity on a logarithmic scale. A Voigt line shape is fitted to the 5 K spectrum, with center frequency 342.6 cm^{-1}. False color plot of the Raman spectra as a function of temperature for (c) VV and (d) VH, with a logarithmic intensity scale. Dashed lines represent T_N and T^*, where a number of new modes appear.

a high-quality single crystal, as seen in other 2D materials belonging to the same space group $C2/m$ (point group C_{2h}) [28,41]. The small energy splitting can be understood as the symmetry-breaking effect of the threefold rotational symmetry of each individual layer due to the monoclinic stacking, with the energy scale proportional to the vdW interaction [41]. In these weakly coupled vdW layers, such monoclinic stacking can be destroyed by handling of the sample [42]. This would manifest as a single broad phonon peak in all polarization configurations. The broadened Raman peak can lead to the interpretation that the bulk crystal exhibits threefold rotational symmetry of the single vdW layer, of point group D_{3d}.

The most dramatic changes can be seen in the frequency region below 220 cm^{-1}. There are several new peaks appearing, in the VV and VH configurations [Figs. 2(c) and 2(d)],

TABLE I. Selected Raman peak frequencies of $CoPS_3$ at 5 K. The experimental Raman peak frequencies at 5 K from fitting the spectra using a Voigt line shape compared with calculated values from density functional theory (DFT) for Raman-active phonons. We assign the DFT-calculated phonon frequencies (and their symmetries) to the experimental value based on its presence in the paramagnetic phase. Zone-folded (ZF) modes calculated frequency and symmetry assignment are intentionally left out due to the multiple number of possible bands that could match the experimental values. *The zone-center magnon modes, M_1 and M_2 have their symmetry assignment based on Fig. 4(a) and Fig. S2 in the Supplemental Material [39].

Label	Symmetry	DFT (cm^{-1})	Expt. (cm^{-1})
P_1	ZF		115.2
P_2	B_g	103.4	116.9
P_3	A_g	104.3	118.8
P_4	B_g	163.4	152.6
P_5	A_g	163.9	158.7
P_6	ZF		163.8
P_7	ZF		198.9
P_8	ZF		218.6
P_9	A_g	218.5	231.8
P_{10}	A_g	233.8	243.1
P_{11}	B_g	267.1	281.4
P_{12}	A_g	268.2	282.3
P_{13}	A_g	369.1	386.1
M_1	A_g*		106.9
M_2	B_g*		187.5

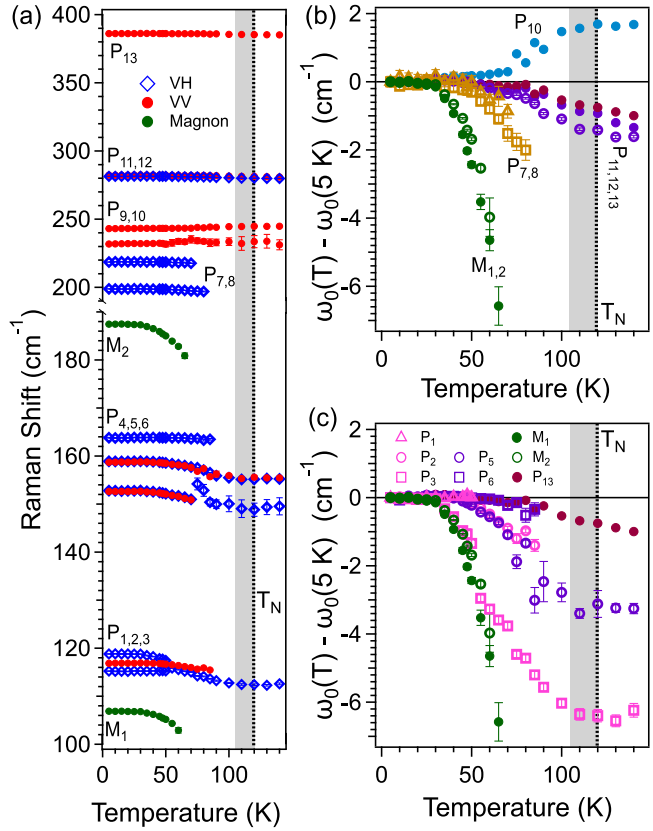

FIG. 3. Temperature-dependent Raman peak frequencies. (a) Peak frequencies of Raman modes in both VV and VH polarization configurations, labeled as $P_{1,...,13}$. The two magnons are once again labeled as $M_{1,2}$. (b) Change in peak frequency as a function of temperature of select modes, showing anomalous (P_{10}), "typical" $P_{11,12,13}$, zone-folding modes $P_{7,8}$, as well as the two magnons $M_{1,2}$. (c) The same change in Raman peak frequency for two peak clusters around 116 cm^{-1} and 157 cm^{-1}, where evidence of hybridization of M_1 and P_3 can be seen by the strong frequency shift of P_3 (hollowed magenta squares) below 50 K, where lattice effects are minimal (as seen in other phonons). The error bars represent 1 standard deviation from the fitting procedure. The Néel transition as well as the critical spin fluctuations [4] are marked by the vertical dashed lines and shaded regions, respectively, in each plot.

while two clusters of peaks around 115 cm^{-1} and 155 cm^{-1} are seemingly formed by the splitting of two significantly broader peaks at high temperature. This behavior is strikingly similar to previous reports on $FePS_3$ [11,12,43,44] as well as $FePSe_3$ [19,20], where two broad Raman scattering peaks above T_N split into multiple sharp Raman modes below T_N. Curiously, the temperature at which these phenomena occur in $CoPS_3$ is well below $T_N \approx 119$ K, which we denote as $T^* \sim 80$ K. It should be noted that in this temperature range, the lattice anharmonic effect is inconsequential. In contrast, for $FePS_3$ with $T_N \approx 118$ K, the new Raman modes appeared only ~8 K below T_N, at ≈110 K.

We fit the Raman spectra using the Voigt line shape; the fitted peak frequencies exhibit a complex temperature dependence visible in Fig. 3(a). The peaks in Fig. 3(a) are labeled corresponding to Table I. In Figs. 3(b) and 3(c), two Brillouin-zone-centered magnon modes, M_1 and M_2, can be seen having the strongest redshift, more than 6 cm^{-1}, as we warm up towards T_N. This behavior is typical of a one-magnon excitation where thermal fluctuations renormalize the magnon energy [12,45]. We also found a broad and weak feature at 343 cm^{-1} (≈42 meV) at 5 K [Figs. 2(b) and 2(d)]. This is consistent with a two-magnon (2M) excitation, similar to the one found in $NiPS_3$ [14,15].

Interestingly, the broad 2M scattering peak at 343 cm^{-1} evolves into a scattering continuum across our measured spectral range above T^* (continuous dark-color background in Fig. 2(d), more clearly seen in Fig. S4 in the Supplemental Material [39]). Drastic changes in the Raman spectrum occur around the same temperature, as mentioned above. The broader spectral linewidth above T^* means a shorter lifetime for the phonon. Such shortened phonon lifetime can be caused by an additional decay pathway, i.e., into the broad magnetic excitation continuum. The correlation between the magnetic scattering continuum and the broad Raman phonon peaks points to significant coupling of the lattice degrees of freedom, represented by the phonons, to the magnetism (see the comparison between the P_5 linewidth and temperature-dependent scattering background in Fig. S4 in the Supplemental Material [39]).

Our analysis of the Raman peak frequencies also reveals at least four other modes that disappear with increasing temperature, i.e., P_1, P_6, P_7, P_8. All of these modes are not measurable above T^*. We attribute these disappearances to the effect of zone folding. The magnetic ordering vector was measured to

be [0 1 0] by neutron scattering [4]. Since the unit cell of space group $C2/m$ is twice that of the primitive cell in the *ab* plane, the propagating vector of [0 1 0] implies that the periodicity of the magnetic structure is twice that of the primitive cell size in the *b* direction. Thus, the magnetic structure provides the necessary crystallographic momentum for zone folding to occur, i.e., Umklapp scattering. The density functional theory (DFT)-calculated normal and zone-folded peaks are included in Table I. Interestingly, we found that the linewidths of the new modes are extremely sharp at low temperature, beyond our instrument's limit of 1.5 cm^{-1} [46].

Figures 3(b) and 3(c) show the difference in frequency of the observed modes to their corresponding frequencies at 5 K as a function of temperature. The Néel transition is marked at 119 K (dashed line), as well as the critical fluctuation region down to 109 K [4] (shaded region). In this temperature range, below 140 K, $P_{11,12,13}$ can be seen exhibiting slight anharmonic frequency softening as the temperature increases to T_N [Fig. 3(b)], with changes in phonon frequency around 1 cm^{-1}. P_{10} shows an anomalous temperature-dependent behavior, with increasing frequency as temperature is increasing. We suspect the renormalization of this phonon frequency is tied to its modulation of the exchange interaction, similar to what has been measured in magnetoelectric materials [47,48]. Interestingly, there is a kink in the temperature-dependent frequency of P_{10} as well as $P_{11,12,13}$, around 70 to 80 K [Fig. 3(b)]. Some of the zone-folded modes, P_7 and P_8, show a slightly stronger temperature dependence than the typical phonons (e.g., P_{11}). It is reasonable to assume that the zone-edge scattering wave vector that allows for the observation of these modes with Raman scattering would be impacted by the magnetic fluctuations near the phase transition.

The fitting results reveal a complex story for the two clusters of modes, $P_{1,2,3}$ and $P_{4,5,6}$. As seen in Fig. 3(a), we assign P_2 and P_6 as the zone-folded modes by their sudden disappearance around T^*. While all of these modes show some frequency changes [Fig. 3(c)], the most notable changes occur at temperatures well below T_N.

The first cluster around 116 cm^{-1} undergoes an apparent "splitting" around 50 K. At high temperature, we can only fit a single peak. We expect there to be a pair of phonons with A_g and B_g symmetry at this frequency. This lack of observation of the second peak is likely due to its weaker signal and significant linewidth broadening. We subtract the high-temperature frequency from the mode at low temperature that produces the least discontinuity, which turns out to be P_3. Below 50 K, we see a strong temperature dependence of P_3's frequency, comparable to the magnons [Fig. 3(c)]. This is the signature of mode repulsion since, at 50 K, the phonon frequency should be frozen. Such an observation is evidence of hybridization between P_3 and M_1. Below 50 K, we see almost identical temperature dependence between M_1 and P_3, where significant change ($> 2\ cm^{-1}$) is followed by a flattening out around 30 K. Similar behavior was observed in $FePSe_3$, where the magnon and phonon are hybridized at low temperature [19,20]. The likely hybridization between M_1 and P_3 is further supported by the fact that they share the same polarization dependence, and hence the same symmetry, at 5 K [Fig. 4(a)].

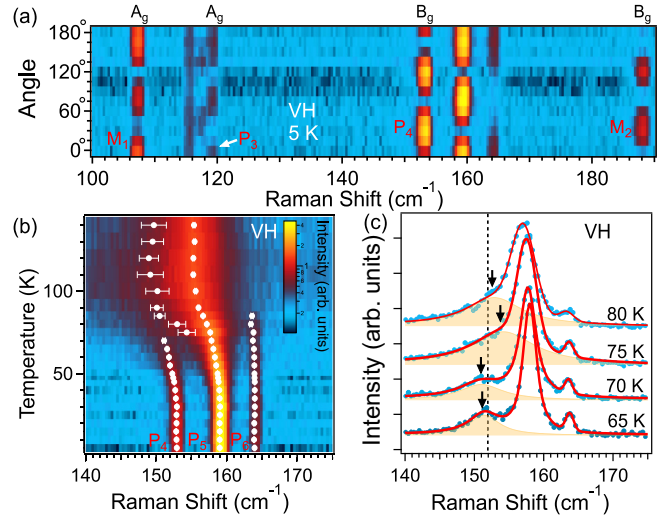

FIG. 4. Symmetry and hybridization between magnons and phonons in $CoPS_3$. (a) False-color plot of polarization-resolved Raman spectra at 5 K, in VH configuration, focusing on two phonon clusters around 116 cm^{-1} and 157 cm^{-1}. The irreducible representation labels of the $2/m$ point group are included to show pairs of modes with the same symmetry: M_1 and P_3 (A_g), M_2 and P_4 (B_g). (b) False-color plot of of the temperature-dependent Raman spectra in VH configuration focused on the cluster at 157 cm^{-1}, with peak fitting results overlayed to show the avoided crossing phenomenon between 70 K and 75 K. The logarithmic-scale intensities are the same for (a) and (b). (c) Select spectra around 75 K in VH configuration with fitted results of three Voigt line-shape peaks (solid lines) and specifically P_4 (shaded peak with arrows representing center frequencies). The vertical dashed line highlights the sudden jump in the center frequency of P_4.

Phenomenologically, the interaction and subsequent mixing between two quantum states can occur if their wave functions overlap. The irreducible representations (Irreps) of the $2/m$ point group, e.g., A_g or B_g, provide a simple way to confirm the possible overlap or orthogonality of these wave functions. Figure 4(a) shows that M_1 (M_2) exhibits a similar polarization dependence to an A_g (B_g) phonon [39]. This implies that the wave function of M_1 transforms like the Irrep A_g, which is orthogonal to B_g. Thus, M_1 is allowed to interact with an A_g phonon (P_3) and not a B_g phonon (P_2). Similarly, M_2 is allowed to interact with a B_g phonon (P_4) and not an A_g phonon (P_5). Indeed, we also discovered the interaction between M_2 and P_4 (and *not* P_5).

In the second cluster around 157 cm^{-1} [Figs. 4(b) and 4(c)], we observed two broad peaks at high temperature. This is predicted from DFT, as we expected a pair of A_g and B_g phonons, P_5 and P_4. At 70 K, the fitting results reveal an avoided crossing behavior in P_4, just before M_2 exhibits measurable intensity at much higher frequency than P_4. The fitting results and false-color spectra are presented in Fig. 4(b), as well as several spectra around the avoided crossing superimposed with individual fitted peaks in Fig. 4(c). These observations indicate that as the magnon frequency changes with temperature and begins to energetically overlap with P_4, an avoided crossing occurs. We estimate the splitting energy to

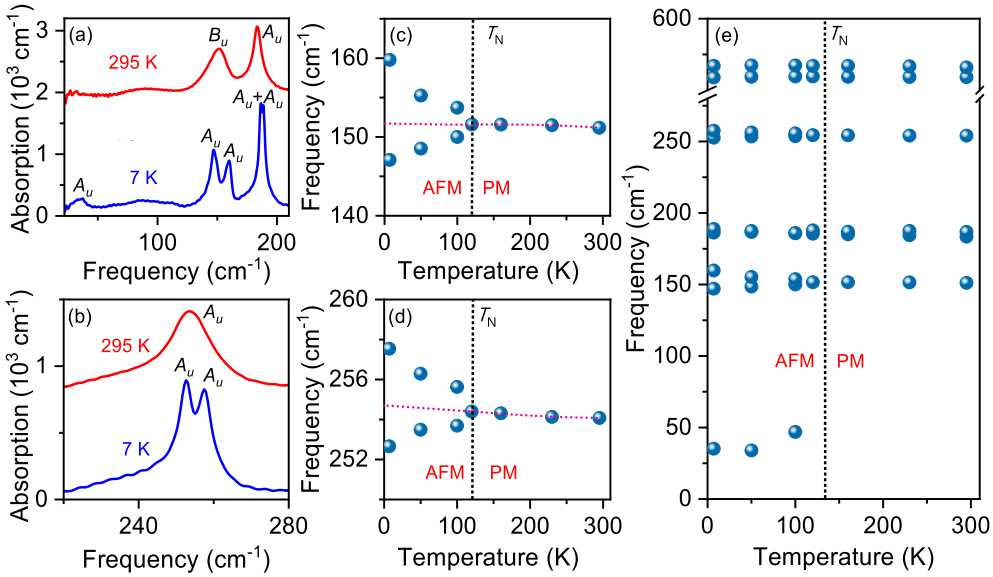

FIG. 5. Infrared response of $CoPS_3$. (a), (b) Close-up view of the infrared absorption in the high- and low-temperature phases, along with (c), (d) frequency vs temperature plots showing spectral changes across the 119 K Néel transition. In (c) and (d), an anharmonic model is fit to the high-temperature phase data. (e) Full view of the frequency vs temperature trends.

be 3 cm^{-1}, or 0.4 meV. The magnon-phonon coupling strength is estimated to be $\approx 3\,\mathrm{cm}^{-1}$ [49], comparable to previously observed values of the coupling energy in 3*d* transition-metal ferro- and ferrimagnetic compounds [50,51].

The infrared absorption data of $CoPS_3$ further support these findings. Here, evidence for spin-phonon coupling is present in the form of peak shifting and splitting of A_u and B_u modes across the 119 K magnetic ordering transition (Fig. 5). Extracting the frequency shifts of these branches from an anharmonic fit of the high-temperature phase data and assuming that the spin-spin correlation function $\langle S_i \cdot S_j \rangle$ goes as $S^2 = (3/2)^2 = 9/4$ in the low-temperature limit, we can estimate the spin-phonon coupling constants (λ's) for the different branches of these modes as $\Delta\omega = \lambda \langle S_i \cdot S_j \rangle$ [48]. We find that the λ's for the two branches of the 151 cm^{-1} A_u symmetry mode below T_N are approximately -2.02 and 3.6 cm^{-1}. The λ's for the two branches of the 252 cm^{-1} B_u symmetry mode are of the order of ± 1 cm^{-1}, respectively. These values are an order of magnitude smaller than what is observed in related Co-containing oxides [48].

A recent study [17] showed a similar deviation from the phonon anharmonicity effects, for inversion-even Raman phonons, due to a general spin-phonon coupling effect, down to 100 K. It should be noted that only the two clusters mentioned above undergo striking changes in linewidth and splitting below T^*. In comparison, the phonons at higher energy remain single peaks with little changes to their frequency and lifetime across T_N. Nonlinear optical spectroscopy measurements have been carried out recently for $FePS_3$ [52] and $CoPS_3$ [53] that reveal coherent spin-lattice coupling in these materials. Specifically, the strong coupling between the spin-orbital electronic excitation of the Co^{2+} to phonon modes at 3.5 THz ($\approx$117 cm^{-1}) and 4.7 THz ($\approx$157 cm^{-1}) seen by [53] further corroborate our finding of the entanglement effect between the spin and lattice in $CoPS_3$.

IV. DISCUSSION

Previously, there has been no clear evidence of a second phase transition or crossover behavior in $CoPS_3$ below T_N from inelastic neutron scattering and magnetic susceptibility [4]. In the present study, the temperature-dependent phonon spectra exhibit splitting of Raman phonon modes, at some intermediate temperature $T^* \sim 80$ K below T_N. Furthermore, we detect no anomaly in the heat capacity between 30 K and 100 K (Fig. S3 in the Supplemental Material [39]). Combined with the lack of a clear lattice symmetry-breaking signature in the high-resolution x-ray data at such a temperature, the data point to a more subtle effect that occurs near T^*. A recent publication on few-layer $NiPS_3$ [13] linked the splitting of the broad Raman phonons as well as the appearance of new peaks at low temperature to the broken threefold rotational symmetry and broken translational symmetry (zone folding) of the individual vdW layer, respectively, caused by the spontaneous long-range magnetic ordering. While, in the few-layers limit, the rotational symmetry-breaking effect of the monoclinic stacking should become less significant, we have no reason to believe that the high-temperature Raman and IR spectra from our bulk sample are from the individual layer responses.

Indeed, we already observed the effect of broken threefold rotational symmetry above T_N [Fig. 2(a)]. Due to this observation, the dramatic differences between the phonon spectrum above and below T^* remain a challenging puzzle to address. In this work, we presented a qualitative picture of spin-lattice coupling based on zone folding, magnon-phonon hybridization, and a broad magnetic scattering continuum that exists only above T^*. The data indicate the coherent coupling between the lattice and magnetic normal modes at low temperature, embodied by the avoided crossing around 75 K (Fig. 4). The microscopic details of these interactions between the lattice and magnetic ground-state excitations remain to be studied. Calculation of the magnon-phonon coupling could be

carried out in the framework of phonon modulation of the exchange pathway [47]. Nevertheless, such unique entanglement between specific crystal-lattice and spin-lattice excitations would imply that at some higher temperature, thermal spin fluctuations can lead to the broadening linewidth of specific phonon modes.

In a recent Raman scattering work by Liu *et al.* [54], a 532 nm laser is used to excited $CoPS_3$ samples with varying thicknesses, from bulk to monolayer, across T_N. Although the bulk room-temperature spectra reported in their work are similar to our observations with a 633 nm laser above T_N, the low-temperature spectra are markedly different. We are able to resolve individual, nonoverlapped peaks, with the full width at half maximum of less than $1.5\,cm^{-1}$ (our instrument's limit) at 25 K. This difference is likely due to both sample quality (see the discussion on monoclinic stacking in the text above) and differences in resolution between the instruments. This ability to finely resolve the Raman peaks allows us to observe the evolution of the broad phonon peaks (above T_N) into the multiple sharp peaks (below T_N). In turn, the rich coupling between the lattice and spin dynamics is revealed in our study.

The various temperature-dependent behaviors described here are not unique to $CoPS_3$. Some can be found in other magnetic $3d$ transition-metal members of the MPX_3 family. However, only in $CoPS_3$ are these spin-lattice effects found together and with significant magnitude, possibly due to the coupled spin and orbital moments in Co^{2+}. Our observations both highlight the complexity of coupled degrees of freedom in real-world quasi-two-dimensional materials, as well as showcase the MPX_3 family as the perfect platform to study these couplings.

V. SUMMARY

In summary, we present a detailed experimental study of the spin and lattice coupling in $CoPS_3$. The bulk characterization results point to a concomitant structural anomaly with the antiferromagnetic transition, indicative of magnetoelastic coupling. While such behavior is typical in the magnetic members of the MPX_3 family [8–10], we also observed abrupt changes to the phonon spectrum around $T^* \sim 80$ K, below $T_N \approx 119$ K. Among the changes is the appearance of new modes, some of which are Brillouin-zone-center magnons [23] and zone-folded phonons due to the magnetism-induced doubling of the unit cell. The latter is confirmed by first-principles calculation. We also discovered the coherent coupling between two pairs of magnons and phonons, at approximately $116\,cm^{-1}$ and $153\,cm^{-1}$. This observation is a telltale sign of the strong entanglement between the crystal lattice and the magnetism in $CoPS_3$. We employed the mode repulsion phenomenology to quantify the observed magnon-phonon coupling effect. Furthermore, we point out the need for a microscopic model that can capture the coupling between the magnetic excitation spectrum and the lattice excitation spectrum in $CoPS_3$, in order to elucidate the coupling effect between spin and lattice in these 2D magnetic materials.

ACKNOWLEDGMENTS

Work at the University of Tennessee (S.S. and J.L.M.) is supported by the Physical Behavior of Materials, Basic Energy Sciences, U.S. Department of Energy (Contract No. DE-SC0023144). Work at the University of Virginia (M.Z. and M.N.A.T.) is supported by the National Science Foundation under Grant No. 2421213. Use of the Advanced Photon Source at Argonne National Laboratory was supported by the U.S. Department of Energy, Office of Science, Office of Basic Energy Sciences, under Contract No. DE-AC02-06CH11357. Work at Oak Ridge National Laboratory was supported by the U.S. Department of Energy, Office of Science, Basic Energy Sciences, Materials Sciences and Engineering Division. The work at AFRL is supported by the Air Force Office of Scientific Research (AFOSR) Grant No. LRIR 23RXCOR003.

Certain trade names and company products are identified in order to adequately specify the experimental procedure. In no case does such identification imply recommendation or endorsement by the National Institute of Standards and Technology, nor does it imply that the products are necessarily the best for the purpose.

Distribution Statement A. Approved for public release: distribution is unlimited. AFRL-2025-2706.

DATA AVAILABILITY

The data that support the findings of this article are not publicly available. The data are available from the authors upon reasonable request.

[1] K. F. Mak, J. Shan, and D. C. Ralph, Probing and controlling magnetic states in 2D layered magnetic materials, Nat. Rev. Phys. **1**, 646 (2019).

[2] M. A. Susner, M. Chyasnavichyus, M. A. McGuire, P. Ganesh, and P. Maksymovych, Metal thio- and selenophosphates as multifunctional van der Waals layered materials, Adv. Mater. **29**, 1602852 (2017).

[3] A. Abragam and B. Bleaney, *Electron Paramagnetic Resonance of Transition Ions* (Oxford University Press, Oxford, 1970).

[4] A. R. Wildes, V. Simonet, E. Ressouche, R. Ballou, and G. J. McIntyre, The magnetic properties and structure of the quasi-two-dimensional antiferromagnet $CoPS_3$, J. Phys.: Condens. Matter **29**, 455801 (2017).

[5] M. Elliot, P. A. McClarty, D. Prabhakaran, R. D. Johnson, H. C. Walker, P. Manuel, and R. Coldea, Order-by-disorder from bond-dependent exchange and intensity signature of nodal quasiparticles in a honeycomb cobaltate, Nat. Commun. **12**, 3936 (2021).

[6] Y. Li, T. T. Mai, M. Karaki, E. V. Jasper, K. F. Garrity, C. Lyon, D. Shaw, T. DeLazzer, A. J. Biacchi, R. L. Dally, D. M. Heligman, J. Gdanski, T. Adel, M. F. Muñoz, A. Giovannone, A. Pawbake, C. Faugeras, J. R. Simpson, K. Ross, N. Trivedi *et al.*, Ring-exchange interaction effects on magnons in the Dirac magnet $CoTiO_3$, Phys. Rev. B **109**, 184436 (2024).

[7] T. T. Mai, Y. Li, K. F. Garrity, D. Shaw, T. DeLazzer, R. L. Dally, T. Adel, M. F. Muñoz, A. Giovannone, C. Lyon, A.

Pawbake, C. Faugeras, F. Le Mardele, M. Orlita, J. R. Simpson, K. Ross, R. V. Aguilar, and A. R. Hight Walker, Spin-orbital–lattice coupling and the phonon Zeeman effect in the Dirac honeycomb magnet $CoTiO_3$, Phys. Rev. B **111**, 104419 (2025).

[8] S. Bjarman, P. Jernberg, and R. Wäppling, $FePS_3$: A first order phase transition in a "two dimensional" antiferromagnet, Hyperfine Interact. **16**, 625 (1983).

[9] P. Jernberg, S. Bjarman, and R. Wäppling, $FePS_3$: A first-order phase transition in a "2D" Ising antiferromagnet, J. Magn. Magn. Mater. **46**, 178 (1984).

[10] Y. Takano, N. Arai, A. Arai, Y. Takahashi, K. Takase, and K. Sekizawa, Magnetic properties and specific heat of MPS_3 (M = Mn, Fe, Zn), J. Magn. Magn. Mater. **272-276**, E593 (2004).

[11] J.-U. Lee, S. Lee, J. H. Ryoo, S. Kang, T. Y. Kim, P. Kim, C.-H. Park, J.-G. Park, and H. Cheong, Ising-type magnetic ordering in atomically thin $FePS_3$, Nano Lett. **16**, 7433 (2016).

[12] A. McCreary, J. R. Simpson, T. T. Mai, R. D. McMichael, J. E. Douglas, N. Butch, C. Dennis, R. V. Aguilar, and A. R. Hight Walker, Quasi-two-dimensional magnon identification in antiferromagnetic $FePS_3$ via magneto-Raman spectroscopy, Phys. Rev. B **101**, 064416 (2020).

[13] Z. Sun, G. Ye, C. Zhou, M. Huang, N. Huang, X. Xu, Q. Li, G. Zheng, Z. Ye, C. Nnokwe, L. Li, H. Deng, L. Yang, D. Mandrus, Z. Y. Meng, K. Sun, C. R. Du, R. He, and L. Zhao, Dimensionality crossover to a two-dimensional vestigial nematic state from a three-dimensional antiferromagnet in a honeycomb van der Waals magnet, Nat. Phys. **20**, 1764 (2024).

[14] S. Rosenblum, A. H. Francis, and R. Merlin, Two-magnon light scattering in the layered antiferromagnet $NiPS_3$: Spin-1/2-like anomalies in a spin-1 system, Phys. Rev. B **49**, 4352 (1994).

[15] K. Kim, S. Y. Lim, J.-U. Lee, S. Lee, T. Y. Kim, K. Park, G. S. Jeon, C.-H. Park, J.-G. Park, and H. Cheong, Suppression of magnetic ordering in XXZ-type antiferromagnetic monolayer $NiPS_3$, Nat. Commun. **10**, 345 (2019).

[16] T. T. Mai, K. F. Garrity, A. McCreary, J. Argo, J. R. Simpson, V. Doan-Nguyen, R. V. Aguilar, and A. R. H. Walker, Magnon-phonon hybridization in 2D antiferromagnet $MnPSe_3$, Sci. Adv. **7**, eabj3106 (2021).

[17] R. Rao, R. Selhorst, R. Siebenaller, A. N. Giordano, B. S. Conner, E. Rowe, and M. A. Susner, Mode-selective spin–phonon coupling in van der Waals antiferromagnets, Adv. Phys. Res. **3**, 2300153 (2024).

[18] S. Liu, A. Granados del Águila, D. Bhowmick, C. K. Gan, T. Thu Ha Do, M. A. Prosnikov, D. Sedmidubský, Z. Sofer, P. C. M. Christianen, P. Sengupta, and Q. Xiong, Direct observation of magnon-phonon strong coupling in two-dimensional antiferromagnet at high magnetic fields, Phys. Rev. Lett. **127**, 097401 (2021).

[19] J. Cui, E. V. Boström, M. Ozerov, F. Wu, Q. Jiang, J.-H. Chu, C. Li, F. Liu, X. Xu, A. Rubio, and Q. Zhang, Chirality selective magnon-phonon hybridization and magnon-induced chiral phonons in a layered zigzag antiferromagnet, Nat. Commun. **14**, 3396 (2023).

[20] J. Luo, S. Li, Z. Ye, R. Xu, H. Yan, J. Zhang, G. Ye, L. Chen, D. Hu, X. Teng, W. A. Smith, B. I. Yakobson, P. Dai, A. H. Nevidomskyy, R. He, and H. Zhu, Evidence for topological magnon–phonon hybridization in a 2D antiferromagnet down to the monolayer limit, Nano Lett. **23**, 2023 (2023).

[21] F. Le Mardelé, A. El Mendili, M. E. Zhitomirsky, I. Mohelsky, D. Jana, I. Plutnarova, Z. Sofer, C. Faugeras, M. Potemski, and M. Orlita, Transverse and longitudinal magnons in the strongly anisotropic antiferromagnet $FePS_3$, Phys. Rev. B **109**, 134410 (2024).

[22] S. Mañas-Valero, T. van der Sar, R. A. Duine, and B. van Wees, Fundamentals and applications of van der Waals magnets in magnon spintronics, Newton **1**, 100018 (2025).

[23] A. R. Wildes, B. Fåk, U. B. Hansen, M. Enderle, J. R. Stewart, L. Testa, H. M. Rønnow, C. Kim, and J.-G. Park, Spin wave spectra of single crystal $CoPS_3$, Phys. Rev. B **107**, 054438 (2023).

[24] K. Van Koughnet, B. Mallett, S. Chong, B. S. Conner, M. A. McGuire, M. A. Susner, and R. G. Buckley, Spin-lattice and spin-electronic interactions in the van der Waals semiconductor $Co_2P_2S_6$, Phys. Rev. B **109**, 165142 (2024).

[25] T. Matsuoka, R. Rao, M. A. Susner, B. S. Conner, D. Zhang, and D. Mandrus, Pressure-induced insulator-to-metal transition in the van der Waals compound $CoPS_3$, Phys. Rev. B **107**, 165125 (2023).

[26] C. Frontera and J. Rodríguez-Carvajal, Fullprof as a new tool for flipping ratio analysis: Further improvements, Phys. B: Condens. Matter **350**, E731 (2004).

[27] Computer code, Rigaku Oxford Diffraction CrysAlis^{Pro}, https://rigaku.com/products/crystallography/x-ray-diffraction/crysalispro.

[28] T. T. Mai, A. McCreary, P. Lampen-Kelley, N. Butch, J. R. Simpson, J.-Q. Yan, S. E. Nagler, D. Mandrus, A. R. Hight Walker, and R. V. Aguilar, Polarization-resolved Raman spectroscopy of α-$RuCl_3$ and evidence of room-temperature two-dimensional magnetic scattering, Phys. Rev. B **100**, 134419 (2019).

[29] P. Hohenberg and W. Kohn, Inhomogeneous electron gas, Phys. Rev. **136**, B864 (1964).

[30] W. Kohn and L. Sham, Self-consistent equations including exchange and correlation effects, Phys. Rev. **140**, A1133 (1965).

[31] A. Togo, First-principles phonon calculations with PHONOPY and PHONO3PY, J. Phys. Soc. Jpn. **92**, 012001 (2023).

[32] P. Giannozzi *et al.*, QUANTUM ESPRESSO toward the exascale, J. Chem. Phys. **152**, 154105 (2020).

[33] K. F. Garrity, J. W. Bennett, K. M. Rabe, and D. Vanderbilt, Pseudopotentials for high-throughput DFT calculations, Comput. Mater. Sci. **81**, 446 (2014).

[34] J. P. Perdew, A. Ruzsinszky, G. I. Csonka, O. A. Vydrov, G. E. Scuseria, L. A. Constantin, X. Zhou, and K. Burke, Restoring the density-gradient expansion for exchange in solids and surfaces, Phys. Rev. Lett. **100**, 136406 (2008).

[35] M. Cococcioni, The LDA+U approach: A simple Hubbard correction for correlated ground states, in *Correlated Electrons: From Models to Materials Modeling and Simulation* (Verlag des Forschungszentrum Jülich, Jülich, Germany, 2012).

[36] A. Togo, L. Chaput, T. Tadano, and I. Tanaka, Implementation strategies in PHONOPY and PHONO3PY, J. Phys.: Condens. Matter **35**, 353001 (2023).

[37] K. Momma and F. Izumi, VESTA3 for three-dimensional visualization of crystal, volumetric and morphology data, J. Appl. Crystallogr. **44**, 1272 (2011).

[38] G. Ouvrard, R. Brec, and J. Rouxel, Structural determination of some MPS_3 layered phases (M = Mn, Fe, Co, Ni and Cd), Mater. Res. Bull. **20**, 1181 (1985).

[39] See Supplemental Material at http://link.aps.org/supplemental/10.1103/nbp7-glqj for the following: I. More information

from single-crystal XRD; II. Group theory phonon analysis; III. Raman tensor and polarized Raman analysis; IV. Heat capacity with dual-slope analysis; and V. Two-magnon scattering and magnetic continuum, which also contains Refs. [14,23,28,45,55–58].

[40] M. J. A. Houmes, G. Baglioni, M. Šiškins, M. Lee, D. L. Esteras, A. M. Ruiz, S. Mañas-Valero, C. Boix-Constant, J. J. Baldoví, E. Coronado, Y. M. Blanter, P. G. Steeneken, and H. S. J. van der Zant, Magnetic order in 2D antiferromagnets revealed by spontaneous anisotropic magnetostriction, Nat. Commun. **14**, 8503 (2023).

[41] D. T. Larson and E. Kaxiras, Raman spectrum of CrI_3: An *ab initio* study, Phys. Rev. B **98**, 085406 (2018).

[42] H. B. Cao, A. Banerjee, J.-Q. Yan, C. A. Bridges, M. D. Lumsden, D. G. Mandrus, D. A. Tennant, B. C. Chakoumakos, and S. E. Nagler, Low-temperature crystal and magnetic structure of α-$RuCl_3$, Phys. Rev. B **93**, 134423 (2016).

[43] M. Balkanski, M. Jouanne, G. Ouvrard, and M. Scagliotti, Effects due to spin ordering in layered MPX_3 compounds revealed by inelastic light scattering, J. Phys. C **20**, 4397 (1987).

[44] M. Scagliotti, M. Jouanne, M. Balkanski, G. Ouvrard, and G. Benedek, Raman scattering in antiferromagnetic $FePS_3$ and $FePSe_3$ crystals, Phys. Rev. B **35**, 7097 (1987).

[45] D. J. Lockwood, M. G. Cottam, V. C. Y. So, and R. S. Katiyar, Raman scattering from one-magnon excitations in FeF_2, J. Phys. C **17**, 6009 (1984).

[46] D. Tuschel, Spectral resolution and dispersion in Raman spectroscopy, Spectroscopy **35**, 9 (2005).

[47] A. B. Sushkov, O. Tchernyshyov, W. Ratcliff, S. W. Cheong, and H. D. Drew, Probing spin correlations with phonons in the strongly frustrated magnet $ZnCr_2O_4$, Phys. Rev. Lett. **94**, 137202 (2005).

[48] K. Park, J. Kim, S. Choi, S. Fan, C. Kim, D. G. Oh, N. Lee, S.-W. Cheong, V. Kiryukhin, Y. J. Choi, D. Vanderbilt, J. H. Lee, and J. L. Musfeldt, Spin-phonon interactions and magnetoelectric coupling in $Co_4B_2O_9$ (B = Nb, Ta), Appl. Phys. Lett. **122**, 182902 (2023).

[49] We estimate the splitting and coupling constant based on the energy deflection of the measured phonon peak. In a coupled two-state system, the maximum splitting is twice that of the coupling constant. Hence, the maximum deflection measured in a single mode is approximately 1/2 of the splitting, which is the coupling constant.

[50] T. D. Kang, E. Standard, K. H. Ahn, A. A. Sirenko, G. L. Carr, S. Park, Y. J. Choi, M. Ramazanoglu, V. Kiryukhin, and S.-W. Cheong, Coupling between magnon and ligand-field excitations in magnetoelectric $Tb_3Fe_5O_{12}$ garnet, Phys. Rev. B **82**, 014414 (2010).

[51] T. V. Brinzari, J. T. Haraldsen, P. Chen, Q.-C. Sun, Y. Kim, L.-C. Tung, A. P. Litvinchuk, J. A. Schlueter, D. Smirnov, J. L. Manson, J. Singleton, and J. L. Musfeldt, Electron-phonon and magnetoelastic interactions in ferromagnetic $Co[\mathbf{N}(CN)_2]_2$, Phys. Rev. Lett. **111**, 047202 (2013).

[52] Emre Ergeçen, B. Ilyas, J. Kim, J. Park, M. B. Yilmaz, T. Luo, D. Xiao, S. Okamoto, J.-G. Park, and N. Gedik, Coherent detection of hidden spin-lattice coupling in a van der Waals antiferromagnet, Proc. Natl. Acad. Sci. USA **120**, e2208968120 (2023).

[53] D. Khusyainov, T. Gareev, V. Radovskaia, K. Sampathkumar, S. Acharya, M. Šiškins, S. Mañas-Valero, B. A. Ivanov, E. Coronado, T. Rasing, A. V. Kimel, and D. Afanasiev, Ultrafast laser-induced spin-lattice dynamics in the van der Waals antiferromagnet $CoPS_3$, APL Mater. **11**, 071104 (2023).

[54] Q. Liu, L. Wang, Y. Fu, X. Zhang, L. Huang, H. Su, J. Lin, X. Chen, D. Yu, X. Cui, J.-W. Mei, and J.-F. Dai, Magnetic order in XY-type antiferromagnetic monolayer $CoPS_3$ revealed by Raman spectroscopy, Phys. Rev. B **103**, 235411 (2021).

[55] M. S. Dresselhaus, G. Dresselhaus, and A. Jorio, *Group Theory: Application to the Physics of Condensed Matter* (Springer Science and Business Media, New York, 2007).

[56] M. I. Aroyo, A. Kirov, C. Capillas, J. M. Perez-Mato, and H. Wondratschek, Bilbao Crystallographic Server. II. Representations of crystallographic point groups and space groups, Acta. Cryst. A **62**, 115 (2006).

[57] A. P. Cracknell, Scattering matrices for the Raman effect in magnetic crystals, J. Phys. C: Solid State Phys. **2**, 500 (1969).

[58] M. G. Cottam, V. So, D. J. Lockwood, R. S. Katiyar, and H. J. Guggenheim, Raman scattering from magnon pair excitations in FeF_2, J. Phys. C: Solid State Phys. **16**, 1741 (1983).